

# Unsupervised Representation Learning for 3D MRI Super Resolution with Degradation Adaptation

Jianan Liu, Hao Li, Tao Huang, *Senior Member, IEEE*, Euijoon Ahn, Kang Han, Adeel Razi, and Wei Xiang, *Senior Member, IEEE*

arXiv:2205.06891v3 [eess.IV] 26 Jan 2023

**Abstract**—High-resolution (HR) MRI is critical in assisting the doctor’s diagnosis and image-guided treatment but is highly time-consuming and costly to acquire. Therefore, deep learning-based super-resolution reconstruction (SRR) has been investigated to generate super-resolution images from low-resolution (LR) images. Training such neural networks requires authentic HR and LR image pairs, which are difficult to acquire due to patient movement during and between the acquisitions of LR and HR images. Rigid movements of hard tissues can be corrected with image registration. In contrast, the alignment of deformed soft tissues is challenging, making it impractical to train neural networks with authentic HR and LR image pairs. Existing studies in the literature focused on SRR using authentic HR images and down-sampled synthetic LR images. Yet, the difference in degradation representations between synthetic and authentic LR images suppresses the quality of SRR from authentic LR images. In this work, we propose a novel Unsupervised Degradation Adaptation Network (UDEAN) to mitigate this problem. Our network consists of the degradation learning network and the SRR network. The degradation learning network down-samples the HR images by addressing the degradation representation of the misaligned or unpaired LR images. The SRR network learns the mapping from the down-sampled HR images to the original ones. Experimental results show that our method outperforms state-of-the-art networks and can potentially be applied in real clinical settings.

**Index Terms**—3D Super Resolution, Degradation Adaptation, Geometric Deformation, Magnetic Resonance Imaging, Unsupervised Learning.

This work has been submitted to the IEEE for possible publication. Copyright may be transferred without notice, after which this version may no longer be accessible.

Jianan Liu and Hao Li contribute equally to the work and are co-first authors. (Corresponding Author: Hao Li)

Jianan Liu is with Vitalent Consulting, Gothenburg, Sweden (email: jianan.liu@vitalent.se).

Hao Li is with the Department of Neuroradiology, University Hospital Heidelberg, Heidelberg, Germany (email: hao.li@med.uni-heidelberg.de).

Tao Huang, Euijoon Ahn and Kang Han are with the College of Science and Engineering, James Cook University, Cairns, Australia (email: tao.huang1@jcu.edu.au; euijoon.ahn@jcu.edu.au; kang.han@my.jcu.edu.au).

Adeel Razi is with Turner Institute for Brain and Mental Health, School of Psychological Sciences, Monash University, Melbourne, Australia (email: adeel.razi@monash.edu).

Wei Xiang is with the School of Computing, Engineering and Mathematical Sciences, La Trobe University, Melbourne, Australia (email: w.xiang@latrobe.edu.au).

## I. INTRODUCTION

HIGH resolution (HR) MRI provides abundant soft tissue contrast and detailed anatomical structures, which assist doctors in accurate diagnosis and image-guided treatment. However, the acquisition of high-resolution images is highly time-consuming and costly. Therefore, supervised and deep learning-based super-resolution reconstruction (SRR) technology has been proposed to accelerate the MRI acquisition in recent years [1]–[9]. Ideally, paired low-resolution (LR) and high-resolution (HR) MRI images can be used for training such neural networks. However, the misalignment is introduced to the HR and LR MRI image pair due to patient movement during and between the image acquisition, even in the same scan session. The misalignment incurs significant errors in the SR image generation, making it unusable in real-world clinical practice.

A straightforward solution is to correct the transformation between misaligned authentic HR and authentic LR images by image registration [12]. Yet image-registration only works for rigid movement of hard tissues, the non-rigid geometric deformation caused by soft tissues movement is hardly handled [13]. Another solution is training the network using authentic HR images and synthetic LR images, where the synthetic LR images are down-sampled using a deterministic down-sampling filter (e.g., Gaussian blur filter) [1], [2], or  $K$ -space truncation from the authentic HR images [3]–[9]. After the training, the authentic LR images, which are acquired separately, are fed in the trained network to reconstruct SR images. Most previous works in MRI SRR followed this routine and designed several different networks: the CSN [1] and the SERAN [2] employed different attention mechanisms into MRI SRR procedure to enhance the feature fusion for the 2D reconstruction procedure; the ReCNN [3], [4] and the DCSR [5] were the first proposed 3D MRI SRR networks; the mDCSRN [6] as an extension of DCSR further facilitated its capability with increased depth and a discriminator; both the deepGG [7], the SSGNN [10] and the SMORE (3D) [11] generated 3D isotropic SR image volume from anisotropic LR images; leveraging of HR reference with different contrast as prior information was also introduced in the MCSR [8] and the MINet [9] to achieve outstanding performance. Besides, TSCRAN [14] achieved comparable performance to the MINet in

3D SRR with single contrast data and a significant reduction of demands on computational resources and inference time.

However, the performance of the aforementioned supervised networks was greatly compromised in real clinical settings due to the degradation shift [15]. In our case, the degradation shift is caused by the different degradation presentations between the authentic and synthetic LR images. More details of the degradation shift will be introduced in the method section. Several unsupervised SRR approaches, proposed in the generic computer vision field by only employing the unpaired LR and HR images for training, can be applied to avoid such degradation shifts in the supervised SRR procedure. ZSSR [16] learns the degradation from LR image to LR image with lower resolution and utilizes such learned degradation to fit the inverse process from LR image to HR image. SMORE(3D) [11] followed the same manner as ZSSR in 3D MRI SRR. HR-Ref-ZSSR [17] chooses to apply the such procedure to MRI image SR with HR reference provided from another modality. ZSSR-GAN [18] implements a similar idea by augmenting the network with a discriminator. Nevertheless, the above approaches still suffer from the degradation shift caused by the inconsistency between learned degradation from LR image to LR image with lower resolution and the degradation from HR image to LR image. Such degradation shift might be mitigated by applying an approach originally designed for transferring the style from one domain to another, such as CycleGAN [19], where the source and target domains are defined, and the images can be transferred between the two domains. Pseudo-SR [20] transfers the target domain LR image to the source domain using the CycleGAN framework and then uses an SR network to reconstruct the SR image in the source domain. Nonetheless, these CycleGAN-based approaches only transfer the images between the source and target domains in the image space rather than the latent feature space. DASR [21], as another state-of-the-art unsupervised learning method, adapts the image space information in two steps: it first calculates a domain distance map besides transferring the source domain HR image to the target domain LR image using a down-sampling network; then, using loss functions guided by the domain distance map, it trains an SR network to transfer the target domain LR picture back to the source domain HR image. However, without the end-to-end training strategy, the model is unlikely to be optimally trained. Furthermore, these domain transfer algorithms are intended for general computer vision SR tasks and are not especially appropriate for MRI SRR.

To address the issues of lacking aligned authentic LR and HR MRI image pairs and the existence of degradation shifts, we propose an unsupervised method that employs either misaligned or unpaired HR and LR images to train the network. The contributions of this work are summarized as follows:

- We propose an end-to-end unsupervised degradation adaptation deep neural network (UDEAN), which adaptively learns the degradation representation between the misaligned or unpaired authentic LR and HR MRI images via a degradation adaptation (DA) mechanism in both the image space and the latent feature space. The combination of DA in both spaces significantly improves the quality of reconstructed SR images rather than DA in

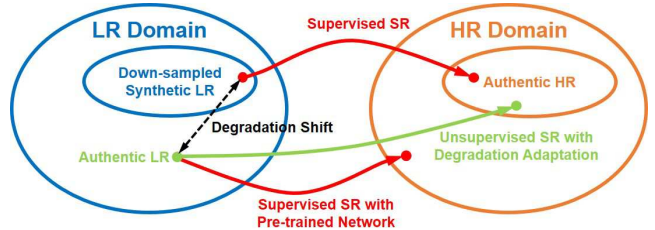


**Fig. 1.** Domain interpretation of differences between supervised and unsupervised SRR. A large degradation shift exists between the SR result and desired HR image, which is caused by applying a supervised network, which is pre-trained with synthetic LR images, to authentic LR images with degradation deviating.

any single space.

- The proposed DA mechanism of UDEAN also shows enhanced performance than the existing domain transfer methods in the literature. Our proposed DA mechanism transfers the LR image with unknown degradation representation to the domain with predefined degradation representation, thus providing minimized errors in the reconstructed SR MRI images.
- The proposed method can be trained with either misaligned or unpaired LR and HR MRI images. Therefore, this proposed method can be applied in real-world clinical settings where perfectly aligned authentic LR and HR MRI image pairs are unavailable.
- Experimental results show that our proposed method has advantages over existing paired supervised by up to 0.022/1.49 in SSIM/PSNR and other unsupervised SR training solutions by up to 0.013/0.75 in SSIM/PSNR across two diverse datasets and two contrasts.

## II. METHODOLOGY

### A. Degradation Shift and SR Reconstruction with Unknown Degradation

Degradation shift, also known as domain gap in the real-world image SRR, was initially noticed in the blind SRR tasks, where the down-sampling parameters of the LR images were unknown [22]. In previous studies of real-world image SRR, the LR images were down-sampled with either a bicubic algorithm or specific Gaussian blurring kernels [22]–[30]. With these down-sampling algorithms, the parameters of the algorithms for the LR images in both training and inference datasets were known. They should be identical to guarantee the performance of the trained network [22]. However, the parameters of the down-sampling algorithms in the real world were normally unknown and very difficult to model [22]. Therefore, it's impossible to guarantee the identical down-sampling for the LR images in both the training dataset and the inference dataset, and the difference between the degradation of the training and inference datasets resulted in a downgraded performance of the trained network in the inference, as shown in Fig. 1.

Similarly, in MRI SRR,  $K$ -space truncation is the most widely-used down-sampling algorithm to generate synthetic LR images [3]–[9]. With this algorithm, an HR image is transformed to its fake  $K$ -space using fast Fourier transformation

(FFT), then the fake  $K$ -space is truncated based on the down-sampling factor. At last, the remained part of the fake  $K$ -space is transformed back to the synthetic LR image using inverse FFT (IFFT). However, the degradation shift between the synthetic and authentic LR images still remained [15]. The method of  $K$ -space truncation is a highly simplified down-sampling model, which simulates the acquisition process of LR images based on the assumption that the  $K$ -spaces of both the HR and the LR images were fully-sampled. However, to shorten the scan time in the clinical measurements, most of the protocols for both LR and HR images acquire  $K$ -spaces, which are under-sampled in several different manners, including partial Fourier in phase-encoding and/or slice-encoding direction, parallel imaging, elliptical  $K$ -space, etc. Most of these under-sampling processes are difficult to simulate accurately since many of the key parameters are unknown. Besides, some other factors also lead to unpredictable differences between the degradation representations of synthetic and authentic LR images, such as the varied signal-to-noise ratio caused by different signal intensity distribution of the  $K$ -spaces or different tuning of transmission/receiving chain.

Therefore, unsupervised SRR can be a promising solution when the degradation shift exists. Several methods have been proposed to solve this problem. These methods can be categorized into three types: the generative network-based domain transfer methods [19]–[21], the blurring kernel-based methods [22]–[28], and contrastive learning [29], [30]. Since the LR MRI images were not down-sampled with either bicubic or Gaussian blurring kernels, the blurring kernel-based methods are incompatible with the MRI SRR. Besides, contrastive learning requires positive and negative training samples, which are difficult to acquire, making this method not applicable in the MRI SRR. Therefore, we developed the degradation adaptation based on the domain transfer method to build our network for SRR from LR images with unknown degradation.

### B. Network Architecture of the UDEAN

Fig. 2 shows the architecture of the proposed UDEAN. The network contains two components: a degradation learning network and an SR Reconstruction network. There are two modules in the degradation learning network. The first module is a degradation mapping module, colored in orange as shown in Fig. 2. This module contains a down-sampling feature extractor and an LR decoder. The second module is an identification module consisting of an LR discriminator and a feature discriminator, as shown in Fig. 2 in blue color. The SRR network includes an LR encoder and an SR decoder (colored in green). It is expected to reconstruct SR images with comparable image quality with the HR images of the source group from the LR images of the target group.

As to the unsupervised training, the image from the source and target groups are used in the training process. The images from the target group are the LR images that will be upsampled to reconstruct the SR images. The images from the source group provide the HR images with the style that the SR images expect. The HR MRI image  $\mathbf{Y}_s$  from the source group and LR MRI image  $\mathbf{X}_t$  from the target group are either misaligned or unpaired, and there is not any ground truth HR image to

calculate any pixel-wise or structural losses with the generated SR image. Noting that misaligned LR and HR images can be considered a special case of unpaired data, where the LR image contains similar structural information as the HR image but is not pixel-wise aligned. Therefore, the training is still not applicable in a supervised manner.

As indicated along the red solid line,  $\mathbf{Y}_s$  is fed to a learnable down-sampling feature extractor to extract the down-sampled feature map  $f_s$  of the source group. Such a feature map contains a generic degradation representation from HR to LR images. Then, the down-sampled LR image  $X_{s \sim t}$ , which contains a comparable degradation representation of the target group LR image  $\mathbf{X}_t$ , is generated by the LR decoder. Then the feature map  $f_{s \sim t \sim s}$  of  $X_{s \sim t}$  is extracted using an LR encoder and generates the SR image  $Y_{s \sim t \sim s}$  using an SR decoder. As the reconstructed SR image  $Y_{s \sim t \sim s}$  and HR image in source group  $\mathbf{Y}_s$  are expected to be identical, and the feature map  $f_{s \sim t \sim s}$  and  $f_s$  should likewise contain comparable context, two-cycle losses are calculated for such purposes. Two consistency losses are also involved in making the training more stable. The LR encoder and LR decoder are trained by minimizing the target group error between  $\mathbf{X}_t$  and the LR image  $\hat{X}_t$  decoded from  $f_t$  along the yellow solid line. Similarly, the down-sampling feature extractor and SR decoder are trained by minimizing the source group error between  $\mathbf{Y}_s$  and SR image  $\hat{Y}_s$  reconstructed from  $f_s$  along the blue solid line.

Since the network is expected to learn the specific degradation representation from the HR images in the source group to the LR images in the target group, an LR discriminator and a feature discriminator are employed. The former is trained to distinguish between the target group LR image  $\mathbf{X}_t$  and the LR image  $X_{s \sim t}$  reconstructed from source group feature. The second discriminator is trained to distinguish between the feature  $f_t$  retrieved from the target group LR and  $f_s$ . The discriminators are trained alternately with the degradation mapping module and SRR network. The UDEAN can adapt from the source group to the specific degradation representation in the target group as long as the discriminators are deceived.

Only the trained LR encoder and SR decoder are required during the inference step, as shown along the yellow dotted line in Fig. 2. The target group LR MRI image  $\mathbf{X}_t$  is encoded into the feature map, then the target group SR MRI image  $\mathbf{Y}_t$  is generated accordingly.

### C. Loss Functions

In our experiments, we employed three types of loss functions, which are the L1 loss, the structural similarity (SSIM) loss [31] [41] and the adversarial loss:

$$L_1(x, y) = \frac{1}{N} \sum_{i=1}^N |x - y| \quad (1)$$

$$L_{SSIM}(x, y) = \frac{1}{N} \sum_{i=1}^N |1 - SSIM(x, y)^2| \quad (2)$$

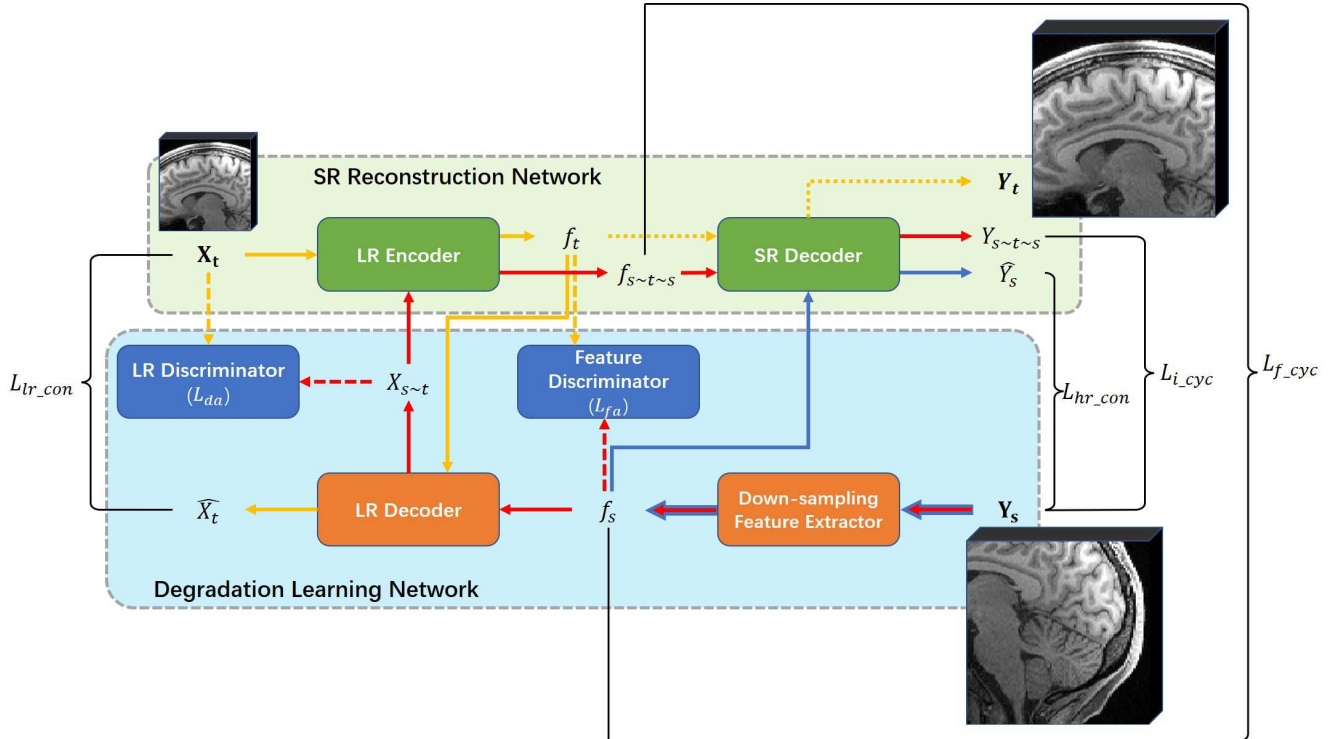


**Fig. 2.** Pipeline of the UDEAN for 3D MRI super-resolution reconstruction. The network is fed with the source group HR image patch  $\mathbf{Y}_s$  and the target group LR image patch  $\mathbf{X}_t$  in training. During the inference, only the target group LR image patch  $\mathbf{X}_t$  is fed in the network, and the SR image patch  $\mathbf{Y}_t$  is reconstructed.

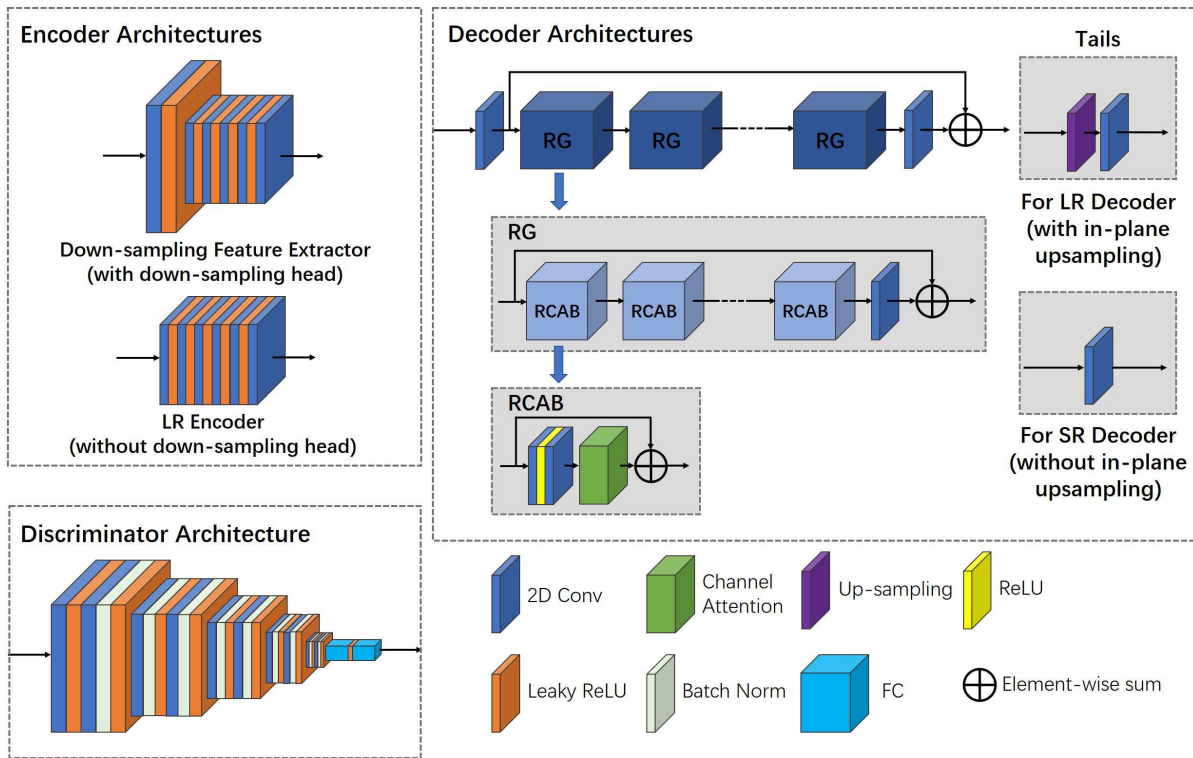


**Fig. 3.** Detailed structures of network components. The encoders are constructed with 6 convolutional layers, each followed by a Leaky ReLU layer. The decoders adopt the TS-RCAN backbone. The VGG network is employed as the discriminators.

$$L_{adv}(x) = \frac{1}{N} \sum_{i=1}^N \sqrt{(D(x) - 1)^2} \quad (3)$$

where the batch size is  $N$ ,  $x$  and  $y$  represent the generated SR image and ground truth HR images, and  $D(\cdot)$  represents the discriminator. To stabilize the training procedure, we use the least square loss [32] for the adversarial loss in our model instead of the negative log-likelihood [33].

As mentioned in the previous section, the two-cycle losses are used to guide the cross-domain restoration of the  $Y_{s \sim t \sim s}$ . The image cycle loss is calculated as a weighted sum of the L1 loss and SSIM loss between  $Y_{s \sim t \sim s}$  and  $Y_s$ , and the adversarial loss of  $Y_{s \sim t \sim s}$ . The feature cycle loss is calculated as the L1 loss between  $f_{s \sim t \sim s}$  and  $f_s$ :

$$L_{i\_cyc} = L_1(Y_{s \sim t \sim s}, Y_s) + \alpha * L_{SSIM}(Y_{s \sim t \sim s}, Y_s) + \beta * L_{adv}(Y_{s \sim t \sim s}) \quad (4)$$

$$L_{f\_cyc} = L_1(f_{s \sim t \sim s}, f_s) \quad (5)$$

Moreover, the consistency losses are used to restrain the restoration of  $\hat{Y}_s$  and  $\hat{X}_t$  within the source and target domain, respectively. They are calculated as a weighted sum of L1, SSIM, and adversarial loss:

$$L_{hr\_con} = L_1(\hat{Y}_s, Y_s) + \alpha * L_{SSIM}(\hat{Y}_s, Y_s) + \beta * L_{adv}(\hat{Y}_s) \quad (6)$$

$$L_{lr\_con} = L_1(\hat{X}_t, X_t) + \alpha * L_{SSIM}(\hat{X}_t, X_t) + \beta * L_{adv}(\hat{X}_t) \quad (7)$$

where  $\alpha$  and  $\beta$  are the weights of the SSIM and adversarial loss, respectively. We set  $\alpha = 0.5$  and  $\beta = 0.01$  in our experiments.

Furthermore, the DA losses in image space ( $L_{da}$ ) and in latent feature space ( $L_{fa}$ ), which stemmed from the LR discriminator and the feature discriminator, are used to guide the network approaching the distributions of the LR images and the features extracted from different domains:

$$L_{da}(X_{s \sim t}, X_t) = \frac{1}{N} \sum_{i=1}^N |D_{da}(X_{s \sim t}) - 0.5| + \frac{1}{N} \sum_{i=1}^N |D_{da}(X_t) - 0.5| \quad (8)$$

$$L_{fa}(f_t, f_s) = \frac{1}{N} \sum_{i=1}^N |D_{fa}(f_t) - 0.5| + \frac{1}{N} \sum_{i=1}^N |D_{fa}(f_s) - 0.5| \quad (9)$$

As a result, the end-to-end training loss for the generators in our network is defined as

$$Loss_{SG} = \lambda_1 * L_{i\_cyc} + \lambda_2 * L_{f\_cyc} + \lambda_3 * L_{hr\_con} + \lambda_4 * L_{lr\_con} + \lambda_5 * L_{da} + \lambda_6 * L_{fa} \quad (10)$$

where  $\lambda_1$  to  $\lambda_6$  are the weights of the loss components. We set  $\lambda_{1,3,4} = 1$  and  $\lambda_{2,5,6} = 0.1$  in our experiments.

#### D. Dataset and Data Pre-processing

In this study, we used two public datasets:

**1) Human Connectome Project (HCP) dataset:** The T1w images from the HCP dataset, which consists of images from 1113 healthy participants [34]. The T1w images were acquired in the sagittal plane with 3D MPRAGE,  $TR = 2400ms$ ,  $TE = 2.14ms$ ,  $TI = 1000ms$ ,  $FA = 8$ ,  $FOV = 224mm$ ,  $rBW = 210Hz/Px$ , the matrix size was  $320 \times 320 \times 256$  with isotropic of resolution  $0.7mm$ , and  $\times 2$  GRAPPA in phase encoding direction was activated. To shorten the training time, we randomly selected 300 participants for our study.

**2) Brain Tumor Segmentation Challenge 2020 (BraTS) dataset:** The contrast-enhanced T1w (T1CE) images from the BraTS dataset, which consists of images from 369 participants with brain tumors [35]–[37]. The T1CE images were acquired in the axial plane, the matrix size was  $240 \times 240 \times 155$  with isotropic resolution  $1.0mm$ . To shorten the training time, we randomly selected 300 participants for our study.

Our experiments involved four data groups: the source, target, validation, and test group. The source and target groups were used to train the neural networks, the validation group was used to monitor the networks' performance during training, and the test group was used to evaluate the networks after training. We randomly selected 120/120/30/30 participants from the HCP dataset for the source, target, validation, and test group. The target group contains only LR images, which were down-sampled from the HR images by 3D  $K$ -space truncation with scale factors of  $2 \times 2 \times 1$  and  $2 \times 2 \times 2$ . The source group contained only HR images from 120 participants and differed between the experiments with misaligned/unpaired HR and LR images. For the unpaired SRR, the participants of the source group were isolated from the other three groups; For the misaligned SRR, the source group shared the same participants with the target group, and the HR images were distorted with certain deformation patterns.

Specifically, for the SRR from misaligned LR and HR image pairs, the participant movement between the acquisition of HR and LR images was simulated by adopting rigid movement and non-rigid geometric deformation to the HR images. The rigid movement was performed by random rotation of the image volumes by 0 to 2 degrees around the head-feet (HF) axis and the left-right (LR) axis and random translation by 0 to 2 voxels in HF and head-feet LR directions. The geometric deformation was achieved by randomly shrinking the whole image volumes by 0 to 2 voxels in anterior-posterior (AP) and LR directions, resulting in a 0.7 to 0.9% of change in the objects' sizes. Each dataset was scaled to the range of 0 to 1, and to save computation resources, the LR and HR images were cropped into 3D patches of sizes  $64 \times 64 \times 3$  and  $128 \times 128 \times 3$  for the scale factor of  $2 \times 2 \times 1$ , and  $64 \times 64 \times 3$  and  $128 \times 128 \times 6$  for the scale factor of  $2 \times 2 \times 2$ , respectively.

#### E. Implementation Details

The detailed structures of our model components are shown in Fig. 3. For the encoders, we used 6 convolution layers with Leaky ReLU between every two layers, and the down-sampling feature extractor down-samples the input HR image to the same size as the LR image. We used the TS-RCAN [14] with 5 residual groups (RG) and 5 residual blocks (RCAB) in each RG as the backbone of the decoders, and VGG [40]

as the discriminator for the UDEAN. TS-RCAN is modified from RCAN [38], [39] to conduct 3D MRI SR tasks with low consumption of computation resources and short inference time.

The networks were trained on a workstation equipped with an Nvidia Quadro A6000. For all deep learning experiments, we used Pytorch 1.9 as the back end. In each training batch, eight LR patches were randomly extracted as inputs. We trained our model for 30 epochs using the ADAM optimizer with  $\beta_1 = 0.9$ ,  $\beta_2 = 0.99$ , and  $\epsilon = 10^{-8}$ , and a Cosine-decay learning rate was applied from  $10^{-4}$  to  $10^{-8}$ . The image pre-processing of down-sampling, deformation, and cropping and the post-processing and metrics calculation were performed with Matlab 2020a. The rigid image registration was performed on Amira 3D with metrics of extended mutual information.

The image quality was evaluated by the most widely-used metrics, signal-to-noise ratio (PSNR) and structure similarity index (SSIM) [1]–[3], [5]–[7], [9]. The higher values of PSNR and SSIM represent better performance. Unlike regular image SRR studied in computer vision research, we didn't adopt any perceptual metrics since structural accuracy is more important than the pure perceptual effect in clinical diagnosis and image-guided treatments.

### III. EXPERIMENTS AND RESULTS

#### A. Ablation Study of the UDEAN

In our experiments, we evaluated our network in various configurations on the same task of SRR for misaligned LR and HR datasets to find the best performance. The effect of DA in the image domain and latent feature domain will be evaluated. Besides, we compared our network to the supervised method using the same backbone network with the misaligned training data to reveal the effect of the degradation of learning modules. As shown in Table I, all the configurations of the UDEAN outperformed the supervised learning using the same generator by over 0.014/0.74 dB in SSIM/PSNR using misaligned LR and HR image from the HCP dataset with the scale factor of  $2 \times 2 \times 2$ . Among the configurations of the UDEAN, the performance was downgraded by 0.009/0.75 dB or 0.002/0.71 dB in SSIM/PSNR when DA in only latent feature space or image space was applied, respectively.

Furthermore, Fig. 4 shows the visual effect of the reconstructed SR images and the error maps to the HR images. The SR image reconstructed by the supervised methods were highly blurry either with or without rigid image registration. On the contrary, the quality of SR images reconstructed by the UDEAN was significantly improved even with DA only in latent feature space or image space. The errors of the reconstructed anatomical structures were further reduced when DA in both domains was applied in the training process.

#### B. Comparison with the State-of-the-Art Unsupervised Methods

We implemented other state-of-the-art unsupervised networks, including ZSSR [16], CycleGAN [19], DASR [21] and PseudoSR [20], as the baseline. All these networks used

the same backbone as the UDEAN for both generators and discriminators and trained with identical training setups, including training datasets and hyperparameters, for fair comparisons. Therefore, the number of network parameters, operations, GPU consumption, and inference time were identical for the inference process for all these networks. The only factor affecting the performance was the pipeline of the whole network for the training process. The numerical results in Table II reveal that the UDEAN outperforms all the above-mentioned networks for MRI SRR from both misaligned and unpaired training data, which are from two datasets with different contrasts and with two scale factors. Specifically, for the HCP dataset and the scale factor of  $2 \times 2 \times 1$ , the ZSSR achieved the best PSNR value. The performance of the UDEAN was comparable to the CycleGAN, with the best SSIM values and the third-best PSNR values for both misaligned and unpaired training data, and the UDEAN outperformed all the other networks. For all the other experiments, the UDEAN outperformed all the other networks with the highest SSIM and PSNR values in most of the cases.

As to the qualitative comparison shown in Fig. 5 for the SRR of the HCP dataset with a scale factor of  $2 \times 2 \times 2$ , ZSSR generated highly blurry images with visible artifacts. The reconstructed image of CycleGAN showed high SSIM and PSNR and improved image quality. However, evident errors on the boundaries of distinct soft tissues were observed in the reconstructed SR images, as shown in the error map. For both PseudoSR and DASR, the inaccuracies of the reconstructed SR images were still massively visible in the error map, although the image quality was acceptable. On the contrary, the reconstructed SR images of the UDEAN achieved higher metrics values and minimized errors. Also shown in Fig. 6 for the SRR with the BraTS dataset and the scale factor of  $2 \times 2 \times 2$ , UDEAN achieved better accuracy than the other networks in the structures of lesions.

### IV. DISCUSSION

#### A. Practicality in Clinical Settings

In real clinical settings, perfectly paired and aligned authentic LR and HR images are difficult to acquire due to patient movements. Besides, in-vivo images are mostly acquired with either LR or HR images in clinical settings because of high time consumption and cost. Lacking paired and aligned LR and HR images raises challenges in implementing supervised SRR methods. Our experimental results revealed that supervised methods could not provide acceptable image quality if the LR and HR images in the training datasets were not perfectly aligned. Even with rigid image registration, the inference results were still unsatisfactory if there was a tiny geometric deformation between the LR and HR images. Therefore, previous studies adopted synthetic LR images generated from HR images with certain down-sampling algorithms as the input of the network [1]–[3], [5]–[7], [9]. However, the degradation shift between the artificial down-sampling and the real degradation from authentic HR to LR images downgrades the performance of the trained networks when they are used for SRR from authentic LR images [15]. Therefore, unsupervised networks can be the possible solution to these problems.

TABLE I

QUANTITATIVE RESULTS OF ABLATION STUDY FOR MRI SRR WITH MISALIGNED LR AND HR IMAGES OF THE HCP DATASET AND SCALE FACTOR OF  $2 \times 2 \times 2$ .

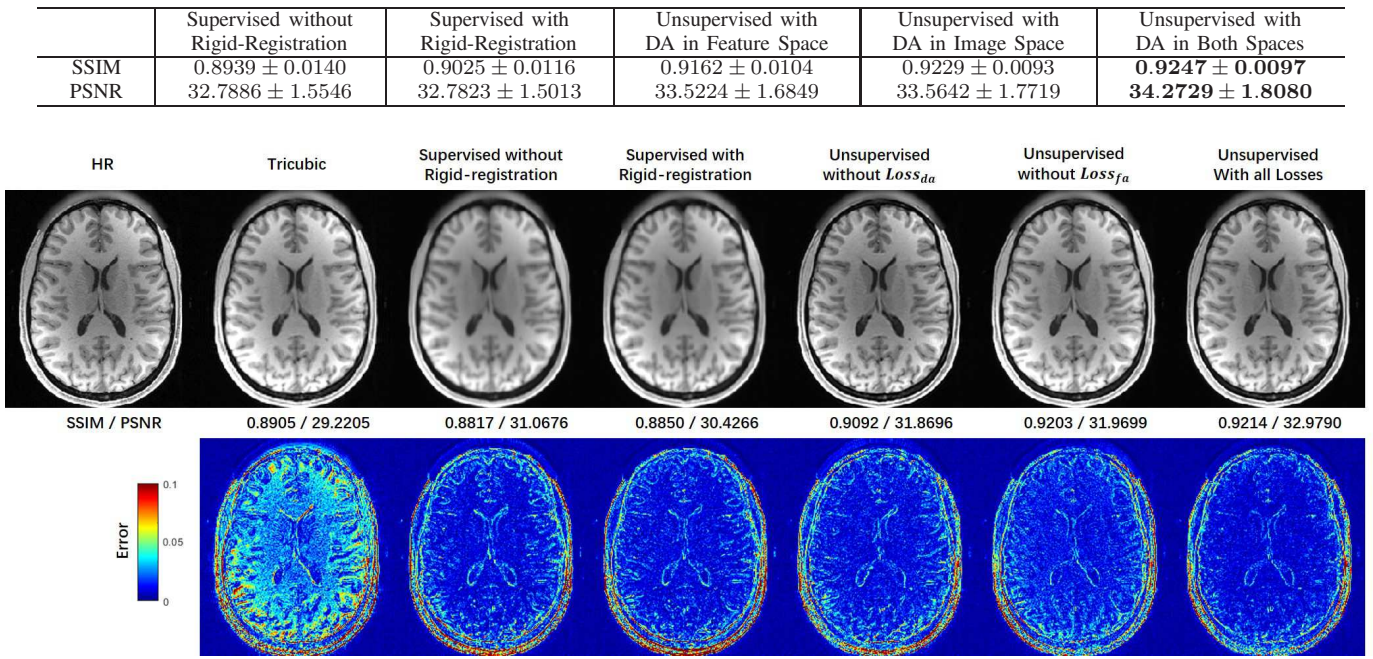


Fig. 4. Comparison of reconstructed SR images and error maps of supervised learning and different configurations of the UDEAN with misaligned LR and HR image pairs of the HCP dataset and the scale factor of  $2 \times 2 \times 2$  in the sagittal plane.

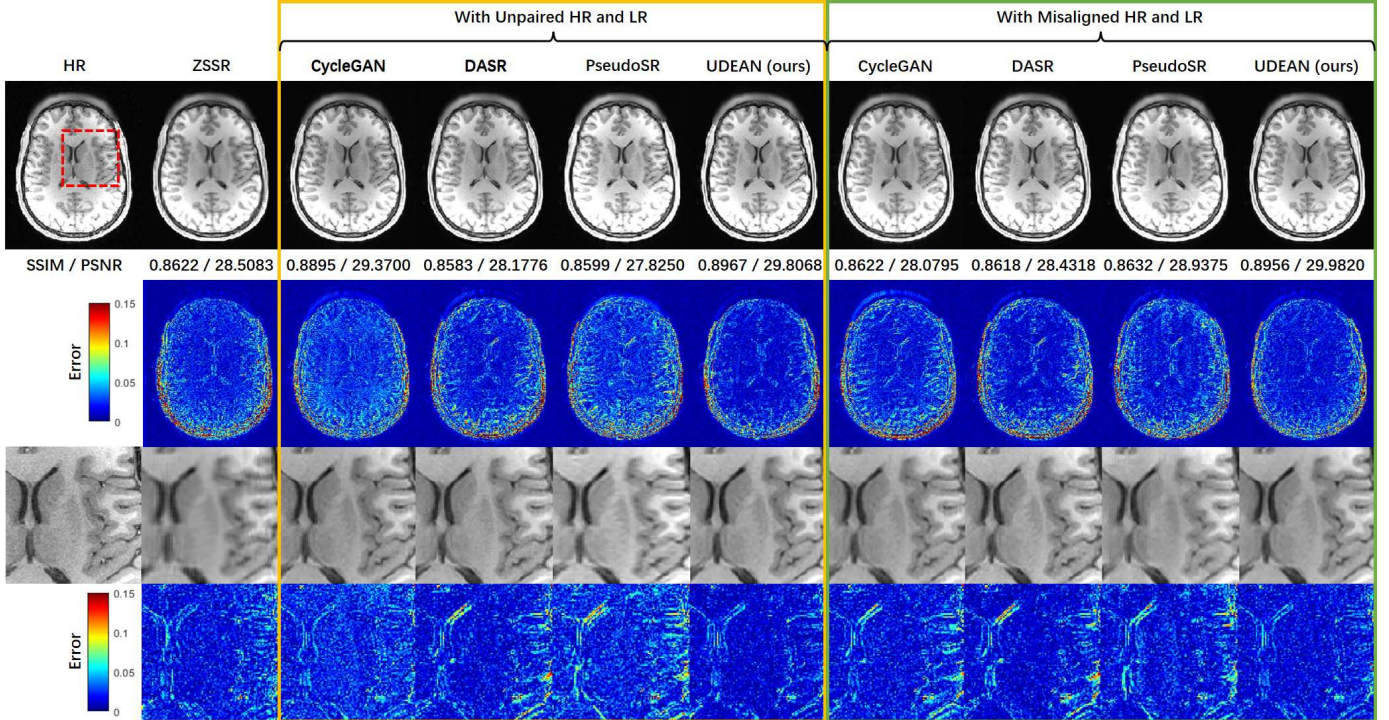


Fig. 5. Qualitative comparison of the UDEAN with the state-of-the-art unsupervised networks in visual effect and error maps in the axial plane with the HCP dataset and the scale factor of  $2 \times 2 \times 2$ .

Previously proposed unsupervised networks were designed for 2D real-world images [16], [19]–[21]. However, medical images are mostly in 3D form, containing through-slice information. Therefore, we adopted the TS-RCAN [14], which is a

low-cost network for 3D SRR with enhanced performance, as the backbone of the UDEAN to process 3D medical images. And comparing to the other unsupervised method, the UDEAN learned the degradation representation in both image space and

TABLE II

QUANTITATIVE COMPARISON WITH THE STATE-OF-THE-ART UNSUPERVISED NETWORKS FOR MRI SRR WITH MISALIGNED AND UNPAIRED LR AND HR IMAGES

Dataset	Scale Factor	Method	Misaligned or Unpaired	SSIM	PSNR
HCP	2 × 2 × 2	Tricubic	N/A	0.8981 ± 0.0106	31.5862 ± 1.8520
		ZSSR [16]	N/A	0.8994 ± 0.0163	33.0213 ± 2.2054
		CycleGAN [19]	Unpaired	0.9164 ± 0.0080	<b>33.9767 ± 1.7352</b>
		DASR [21]	Unpaired	0.8931 ± 0.0094	32.3309 ± 1.4671
		Pseudo SR [20]	Unpaired	0.8931 ± 0.0116	31.0407 ± 1.8816
		UDEAN (ours)	Unpaired	<b>0.9242 ± 0.0083</b>	33.5159 ± 1.7234
	2 × 2 × 1	CycleGAN [19]	Misaligned	0.9226 ± 0.0096	34.2728 ± 1.8235
		DASR [21]	Misaligned	0.8946 ± 0.0091	32.2544 ± 1.4658
		Pseudo SR [20]	Misaligned	0.8962 ± 0.0086	32.0267 ± 1.5950
		UDEAN (ours)	Misaligned	<b>0.9247 ± 0.0097</b>	<b>34.2729 ± 1.8080</b>
		Tricubic	N/A	0.9227 ± 0.0088	33.6545 ± 1.8492
		ZSSR [16]	N/A	0.9412 ± 0.0106	<b>36.0848 ± 2.4098</b>
BraTS	2 × 2 × 2	CycleGAN [19]	Unpaired	0.9317 ± 0.0085	<b>35.7817 ± 1.9124</b>
		DASR [21]	Unpaired	0.9137 ± 0.0084	33.6732 ± 1.4502
		Pseudo SR [20]	Unpaired	0.9244 ± 0.0076	33.8122 ± 1.6044
		UDEAN (ours)	Unpaired	<b>0.9371 ± 0.0078</b>	35.1688 ± 1.8195
		CycleGAN [19]	Misaligned	0.9425 ± 0.0078	<b>35.7028 ± 2.2348</b>
		DASR [21]	Misaligned	0.9192 ± 0.0082	33.9043 ± 1.6386
		Pseudo SR [20]	Misaligned	0.9228 ± 0.0080	34.0500 ± 1.6694
		UDEAN (ours)	Misaligned	<b>0.9455 ± 0.0072</b>	35.5182 ± 2.2839
	2 × 2 × 1	Tricubic	N/A	0.9073 ± 0.0196	31.2470 ± 1.9187
		ZSSR [16]	N/A	0.9001 ± 0.0464	29.6156 ± 3.1528
		CycleGAN [19]	Unpaired	0.9304 ± 0.0135	30.3970 ± 1.8609
		DASR [21]	Unpaired	0.9334 ± 0.0141	30.5198 ± 2.0642
		Pseudo SR [20]	Unpaired	0.8978 ± 0.0129	26.4210 ± 0.8741
		UDEAN (ours)	Unpaired	<b>0.9435 ± 0.0127</b>	<b>31.1462 ± 2.2632</b>
		CycleGAN [19]	Misaligned	0.9433 ± 0.0157	31.3131 ± 2.6067
		DASR [21]	Misaligned	0.9377 ± 0.0151	31.1546 ± 2.0495
		Pseudo SR [20]	Misaligned	0.9378 ± 0.0150	31.0804 ± 1.9391
		UDEAN (ours)	Misaligned	<b>0.9513 ± 0.0133</b>	<b>32.0435 ± 2.2796</b>
		Tricubic	N/A	0.9299 ± 0.0151	34.8846 ± 2.2722
		ZSSR [16]	N/A	0.9514 ± 0.0156	33.2469 ± 3.6422
	2 × 2 × 1	CycleGAN [19]	Unpaired	<b>0.9583 ± 0.0160</b>	35.3937 ± 2.8132
		DASR [21]	Unpaired	0.9462 ± 0.0149	34.4395 ± 1.8905
		Pseudo SR [20]	Unpaired	0.9397 ± 0.0150	34.0382 ± 1.9015
		UDEAN (ours)	Unpaired	0.9551 ± 0.0166	<b>35.4973 ± 2.2433</b>
		CycleGAN [19]	Misaligned	0.9601 ± 0.0159	36.4836 ± 2.7863
		DASR [21]	Misaligned	0.9461 ± 0.0167	34.5953 ± 2.0557
		Pseudo SR [20]	Misaligned	0.9463 ± 0.0162	34.5560 ± 1.9037
		UDEAN (ours)	Misaligned	<b>0.9629 ± 0.0163</b>	<b>36.7631 ± 2.3787</b>

the latent feature space, thus achieving better performance.

### B. Effect of Degradation Representation Learning

The degradation representation learning of the UDEAN was a specific type of domain adaptation, which transferred HR images of the source domain to the LR images of the target domain. The ablation study revealed the effects of domain adaptations, which guided the network to learn the degradation representation in both image and latent feature space. The experimental results showed the advantage of UDEAN to the supervised learning approach on misaligned LR and HR images. When the LR and HR images of the training datasets were not perfectly aligned, the supervised methods failed to provide acceptable image quality. Besides, the ablation study also revealed the effect of degradation representation learning in both image and latent feature space. The network could reconstruct the SR images without either  $Loss_{da}$  or  $Loss_{fa}$ . However, the absence of  $Loss_{da}$  or  $Loss_{fa}$  downgraded the performance of the network, showing the benefit of degradation representation learning in both the image space and the latent feature space.

### C. Comparison of Different Domain Transfer Strategies

Regarding the other state-of-the-art unsupervised networks, the ZSSR, as a network without domain transfer, learned the degradation representation between LR images and the lower resolution images, which were down-sampled from LR images, and used the learned degradation representation to reconstruct the SR images from the LR images [16]. However, there was a large gap between the learned degradation and the degradation from HR images to the LR images, thus leading to downgraded performance, particularly with large-scale factors.

Most unsupervised networks with domain transfer are derived from the CycleGAN. CycleGAN was designed to transfer images between different styles [19], and it could be implemented with an up-sampling network and a down-sampling network to transfer the LR and HR images between the source domain and target domain. Despite the high SSIM and PSNR values, the CycleGAN learned the degradation representation in the image space to reconstruct the SR images [19]. However, due to the absence of degradation representation in the latent feature space, errors on the boundaries of distinct soft tissues were observed in the reconstructed SR images. As the

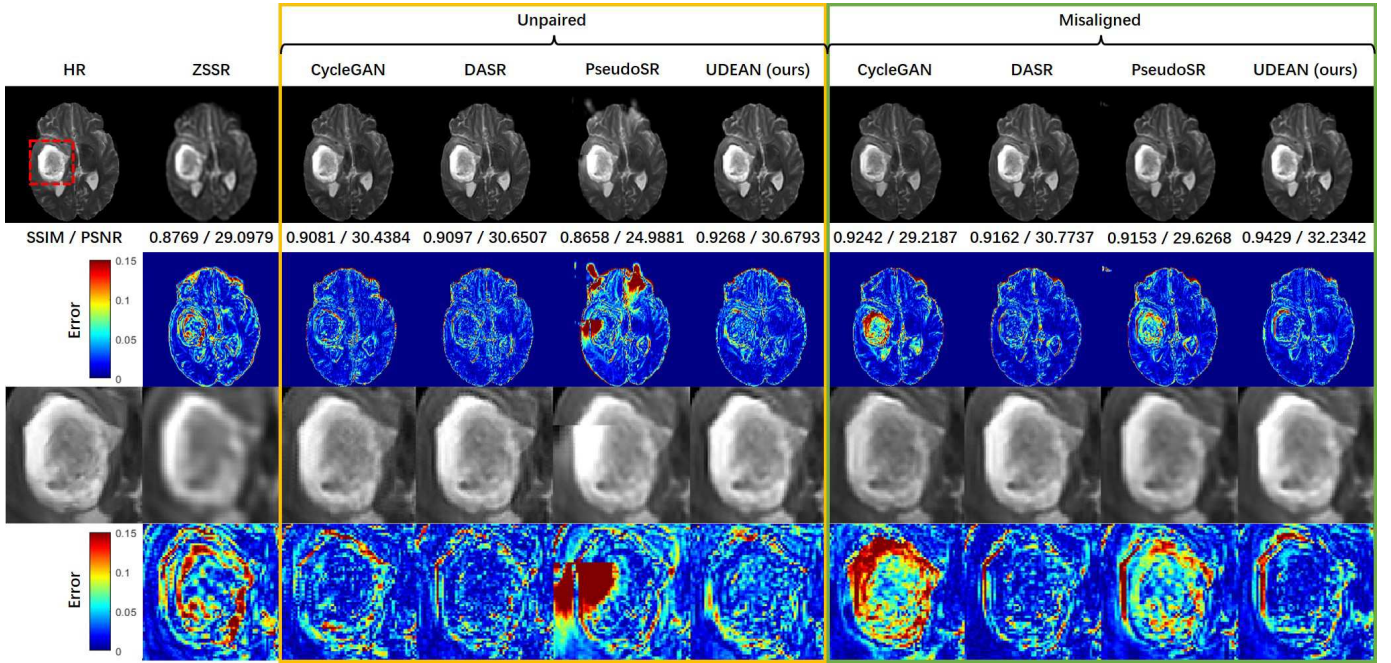


**Fig. 6.** Qualitative comparison of the UDEAN with the state-of-the-art unsupervised networks in visual effect and error maps in the axial plane with the BraTS dataset and the scale factor of  $2 \times 2 \times 2$ .

degradation representations from the unpaired or misaligned HR to the LR images were more complex for the voxels on the boundaries of distinct soft tissues than the voxels inside the soft tissues, the geometric accuracy of boundaries of different soft tissues was reduced with the CycleGAN. Such geometric inaccuracy could result in inaccurate surgery or therapy doses, indicating that the approach is less applicable in real clinics.

As one of the most recent unsupervised SR approach, the DASR learned the degradation representation by down-sample the HR images of the source domain to the LR images in the target domain, and domain distance maps in the image space were generated simultaneously, which were subsequently used to reconstruct SR images [21]. However, this learning strategy was not in an end-to-end fashion, making this network difficult to be trained and optimized, and the learned degradation representation fitted the reconstruction procedure hardly. As a result, the inaccuracies in the DASR's reconstructed SR MRI images are still massively visible.

The PseudoSR is another latest approach to an unsupervised SRR network. It transferred the LR image of the target domain to the source domain, where the LR images were downgraded from HR images with a predefined algorithm. Then the SR images were reconstructed from down-sampled LR images [20]. The experimental results showed that the PseudoSR could achieve neither high metrics values nor satisfactory qualitative image quality. Despite the adaptation of latent feature space, another main difference between the UDEAN and the PseudoSR was that the UDEAN transferred the source domain HR images to the target domain and learned the mapping of the LR images from the target domain to the HR images in the source domain. On the contrary, the PseudoSR transferred the target domain LR images to the source domain and learned the mapping of the LR images from the source

domain to the HR images in the source domain. The ablation study results showed the advantage of the former scheme even with the absence of feature space adaptation.

#### D. Limitations and Future Works

Despite the promising results of the UDEAN, there were still certain limitations to this study. We only tested the UDEAN on MR images of brains, where the geometric deformation is normally mild in real clinics, and the LR images were synthetically generated from HR images. Abdominal and musculoskeletal imaging normally suffer from more severe geometric deformation of soft tissues due to irresistible patient movements. Thus, the UDEAN can be the best solution in these scenarios. However, public datasets containing authentic LR and HR images of abdominal and musculoskeletal imaging are unavailable. Therefore the misaligned or unpaired LR and HR images still need to be artificially generated. Besides, this study focused on investigating the potential of SRR using networks trained by misaligned or unpaired LR and HR images, the datasets we used in our experiments were still applicable to our experiments. In our future study, the performance of the UDEAN trained with authentic LR and HR images will be investigated.

## V. CONCLUSION

In this manuscript, we propose the UDEAN as an unsupervised degradation adaption network that adaptively learns the degradation representation between misaligned or unpaired LR and HR MRI data in both image and latent feature spaces. The UDEAN applies SRR in an end-to-end fashion, making the network easy to train and optimize. The DA mechanism adopted by the UDEAN also shows advantages over the previously used domain transfer methods, thus minimizing errors

in the reconstructed SR images. Our experimental results showed that the UDEAN alleviated the problem of lacking paired authentic LR and HR images, achieved enhanced image quality for SRR and outperformed the other state-of-the-art networks. Therefore, the UDEAN is a promising solution for SRR in clinical settings when perfectly aligned LR and HR image pairs are unavailable.

## REFERENCES

- [1] X. Zhao, Y. Zhang, T. Zhang, and X. Zou, "Channel splitting network for single MR image super-resolution," *IEEE Trans. Image Process.*, vol. 28, no. 11, pp. 5649–5662, 2019.
- [2] Y. Zhang, K. Li, K. Li, and Y. Fu, "MR image super-resolution with squeeze and excitation reasoning attention network," *Proc. IEEE/CVF Conf. Comput. Vis. Pattern Recognit. (CVPR)*, Jun. 2021, pp. 13425–13434.
- [3] C. H. Pham, A. Ducournau, R. Fablet, and F. Rousseau, "Brain MRI super-resolution using deep 3D convolutional networks," *Proc. IEEE Int. Symp. Biomed. Imag.*, Apr. 2017, pp. 197–200.
- [4] C. H. Pham *et al.*, "Multiscale brain MRI super-resolution using deep 3D convolutional networks," *Comput. Med. Imaging. Graph.*, vol. 77, 101647, 2019.
- [5] Y. Chen, Y. Xie, Z. Zhou, F. Shi, A. G. Christodoulou, and D. Li, "Brain MRI super resolution using 3D deep densely connected neural networks," *Proc. IEEE Int. Symp. Biomed. Imag.*, Apr. 2018, pp. 739–742.
- [6] Y. Chen, F. Shi, A. G. Christodoulou, Y. Xie, Z. Zhou, and D. Li, "Efficient and accurate MRI super-resolution using a generative adversarial network and 3D multi-level densely connected network," *Proc. Int. Conf. Med. Image Comput. Comput.-Assist. Intervent.*, Sep. 2018, pp. 91–99.
- [7] Y. Sui, O. Afacan, A. Gholipour, and S. K. Warfield, "Learning a gradient guidance for spatially isotropic MRI super-resolution reconstruction," *Proc. Int. Conf. Med. Image Comput. Comput.-Assist. Intervent.*, Oct. 2020, pp. 136–146.
- [8] Q. Lyn *et al.*, "Multi-Contrast Super-Resolution MRI Through a Progressive Network," *IEEE Trans. Med. Imag.*, vol. 39, no. 9, pp. 2738–2749, 2020.
- [9] C. Feng, H. Fu, S. Yuan, and Y. Xu, "Multi-contrast mri super-resolution via a multi-stage integration network," *Proc. Int. Conf. Med. Image Comput. Comput.-Assist. Intervent.*, Sep. 2021, pp. 140–149.
- [10] Z. Sui, O. Afacan, C. Jaimes, A. Gholipour, and S. K. Warfield, "Scan-Specific Generative Neural Network for MRI Super-Resolution Reconstruction," *IEEE Trans. Med. Imag.*, vol. 41, no. 6, pp. 2738–2749, 2022.
- [11] C. Zhao, B. E. Dewey, D. L. Pham, P. A. Calabresi, D. S. Reich, and J. L. Prince, "SMORE: A Self-Supervised Anti-Aliasing and Super-Resolution Algorithm for MRI Using Deep Learning," *IEEE Trans. Med. Imag.*, vol. 40, no. 3, pp. 805–817, 2021.
- [12] Y. Sui, O. Afacan, A. Gholipour, and S. K. Warfield, "MRI super-resolution through generative degradation learning," *Proc. Int. Conf. Med. Image Comput. Comput.-Assist. Intervent.*, Sep. 2021, pp. 430–440.
- [13] C. Komninos *et al.*, "Intra-operative oct (ioct) image quality enhancement: a super-resolution approach using high quality ioct 3d scans," *Ophthalmic Medical Image Analysis (OMIA)*, vol. 12970, 2021, pp. 21–31.
- [14] H. Li and J. Liu, "3D High-Quality Magnetic Resonance Image Restoration in Clinics Using Deep Learning," 2021, *arXiv:2111.14259*.
- [15] S. Laguna *et al.*, "Super-resolution of portable low-field MRI in real scenarios: integration with denoising and domain adaptation," *Proc. Medical Imaging with Deep Learning*, Apr. 2022.
- [16] A. Shocher, C. Nadav Cohen, and I. Michal, "“zero-shot” super-resolution using deep internal learning," *Proc. IEEE/CVF Conf. Comput. Vis. Pattern Recognit. (CVPR)*, Jun. 2018, pp. 3118–3126.
- [17] Y. Iwamoto, K. Takeda, Y. Li, A. Shiino, and Y. Chen, "Unsupervised MRI Super-Resolution Using Deep External Learning and Guided Residual Dense Network with Multimodal Image Priors," 2020, *arXiv:2008.11921*.
- [18] J. Cui, K. Gong, P. Han, H. Liu, and Q. Li, "Unsupervised arterial spin labeling image superresolution via multiscale generative adversarial network," *Med. Phys.*, vol. 49, no. 4, pp. 2373–2385, 2022.
- [19] J. Zhu, T. Park, P. Isola, and A. A. Efros, "Unpaired image-to-image translation using cycle-consistent adversarial networks," *Proc. IEEE/CVF Conf. Comput. Vis. Pattern Recognit. (CVPR)*, Jul. 2017, pp. 2223–2232.
- [20] S. Maeda, "Unpaired image super-resolution using pseudo-supervision," *Proc. IEEE/CVF Conf. Comput. Vis. Pattern Recognit. (CVPR)*, Jun. 2020, pp. 291–300.
- [21] Y. Wei, S. Gu, Y. Li, R. Timofte, L. Jin, and H. Song, "Unsupervised real-world image super resolution via domain-distance aware training," *Proc. IEEE/CVF Conf. Comput. Vis. Pattern Recognit. (CVPR)*, Jun. 2021, pp. 13385–13394.
- [22] A. Liu, Y. Liu, J. Gu, Y. Qiao, and C. Dong, "Blind image super-resolution: A survey and beyond," *IEEE Trans. Pattern Anal. Mach. Intell.*, 2022, doi: 10.1109/TPAMI.2022.3203009.
- [23] J. Gu, H. Lu, W. Zuo, and C. Dong, "Blind super-resolution with iterative kernel correction," *Proc. IEEE/CVF Conf. Comput. Vis. Pattern Recognit. (CVPR)*, Jun. 2019, pp. 1604–1613.
- [24] L. Xie, X. Wang, C. Dong, Z. Qi, and Y. Shan, "Finding discriminative filters for specific degradations in blind super-resolution," *Proc. Adv. Neural Inf. Process. Syst.*, vol. 34, 2021, pp. 51–61.
- [25] Z. Hui, J. Li, X. Wang, and X. Gao, "Learning the non-differentiable optimization for blind super-resolution," *Proc. IEEE/CVF Conf. Comput. Vis. Pattern Recognit. (CVPR)*, Jun. 2021, pp. 2093–2102.
- [26] M. Yamac, A. Baran, and N. Aakif, "Kernelnet: A blind super-resolution kernel estimation network," *Proc. IEEE/CVF Conf. Comput. Vis. Pattern Recognit. (CVPR)*, Jun. 2021, pp. 453–462.
- [27] K. Zhang, J. Liang, L. Van Gool, and R. Timofte, "Designing a practical degradation model for deep blind image super-resolution," *Proc. IEEE Int. Conf. Comput. Vis. (ICCV)*, Oct. 2021, pp. 4791–4800.
- [28] W. Zhang, G. Shi, Y. Liu, C. Dong, and X. Wu, "A Closer Look at Blind Super-Resolution: Degradation Models, Baselines, and Performance Upper Bounds," *Proc. IEEE/CVF Conf. Comput. Vis. Pattern Recognit. (CVPR)*, Jun. 2022, pp. 527–536.
- [29] L. Wang *et al.*, "Unsupervised degradation representation learning for blind super-resolution," *Proc. IEEE Int. Conf. Comput. Vis. (ICCV)*, Oct. 2021, pp. 10581–10590.
- [30] J. Zhang, S. Lu, F. Zhan, and Y. Yu, "Blind image super-resolution via contrastive representation learning," 2021, *arXiv:2107.00708*.
- [31] E. M. Masutani, B. Naeim, and H. Albert, "Deep learning single-frame and multiframe super-resolution for cardiac MRI," *Radiology*, vol. 295, no. 3, pp. 552–561, 2020.
- [32] X. Mao, Q. Li, H. Xie, R. Y. K. Raymond, and Z. Wang, "Multi-class generative adversarial networks with the L2 loss function," 2016, *arXiv:1611.04076*.
- [33] I. Goodfellow *et al.*, "Generative adversarial networks," *Commun. ACM*, vol. 63, no. 11, pp. 139–144, 2020.
- [34] D. C. Van Essen *et al.*, "The WU-Minn human connectome project: an overview," *Neuroimage*, vol. 80 pp. 62–79, 2013.
- [35] B. Menze *et al.*, "The multimodal brain tumor image segmentation benchmark (BRATS)," *IEEE Trans. Med. Imag.*, vol. 34, no. 10, pp. 1993–2024, 2014.
- [36] C. T. Lloyd, S. Alessandro, and A. J. Tatem, "High resolution global gridded data for use in population studies," *Sci. Data*, vol. 4, no. 1, pp. 1–17, 2017.
- [37] S. Bakas *et al.*, "Identifying the best machine learning algorithms for brain tumor segmentation, progression assessment, and overall survival prediction in the BRATS challenge," 2018, *arXiv:1811.02629*.
- [38] Y. Zhang, K. Li, K. Li, L. Wang, B. Zhong, and Y. Fu, "Image super-resolution using very deep residual channel attention networks," *Proc. Eur. Conf. Comput. Vis.*, Sep. 2018, pp. 286–301.
- [39] Z. Lin *et al.*, "Revisiting rean: Improved training for image super-resolution," 2022, *arXiv:2201.11279*.
- [40] K. Simonyan, and Z. Andrew, "Very deep convolutional networks for large-scale image recognition," 2014, *arXiv:1409.1556*.
- [41] Z. Wang, A. C. Bovik, H. R. Sheikh, and E. P. Simoncelli, "Image quality assessment: from error visibility to structural similarity," *IEEE Trans. Image Process.*, vol. 13, no. 4, pp. 600–612, 2004.